Volume 64, Number 5, September 2012   ISSN 0898-1221

An International Journal

computers & mathematics

with applications

Editor-in-Chief: Leszek F. Demkowicz

ADVANCED TECHNOLOGIES IN COMPUTER,
CONSUMER AND CONTROL
Guest Editors
DR. TZUU-HSENG S. LI
DR. HER-TERNG YAU
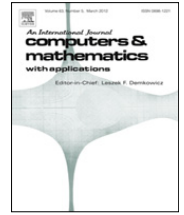
A two-mode six-DOF motion system based on a ball-joint-like spherical motor for haptic applications

Kun Bai [a], Jingjing Ji [b], Kok-Meng Lee [a,b,c,*], Shuyou Zhang [b]

[a] *Woodruff School of Mechanical Engineering, Georgia Institute of Technology, Atlanta, GA 30332, USA*
[b] *Department of Mechanical Engineering, Zhejiang University, Hangzhou 310027, China*
[c] *School of Mechanical Engineering, Huazhong University of Science and Technology, Wuhan 430074, China*

ARTICLE INFO

ABSTRACT

A ball-joint-like spherical motor capable of offering smooth, continuous multi-DOF motion is presented as an alternative design for haptic applications. With a two-mode configuration, this device can be operated as a joystick manipulating a target in six degrees-of-freedom (DOF), and provides realistic force/torque feedback in real-time. Utilizing the magnetic field measurements, the orientation and the torque-to-current coefficients can be computed in parallel; this novel scheme greatly improves the sampling rate as well as reduces error accumulation commonly found in multi-DOF robotic devices. Of particular interest here is to explore this two-mode design in a computer-aided virtual environment. As an intuitive illustration, the disassembly process of a snap-fit (consisting of a typical cantilever hook and a wedge-shaped end) is simulated, where the two-mode permanent magnet spherical motor haptic device is incorporated as an interfacing device that receives motion commands from a virtual design environment and delivers torque feedback to the designer/user.

© 2012 Elsevier Ltd. All rights reserved.

1. Introduction

Haptic devices, which have the capabilities to provide realistic force/tactile feedback to human operators in a virtual environment, play an increasingly important role in training stages in many fields. With the rapid development of computer technology and mechatronics, novel applications of haptic devices can be found in both traditional and emerging industries including robotic automation, medical operations and more recently snap-fit design with haptic device in the loop [1–4].

Traditional haptic devices are typically serial or parallel mechanisms driven by single-axis motors (along with external position encoders and force/torque measuring devices as feedback sensors) to achieve multi-DOF motion in the working space [5–7]. Cumbersome serial or parallel configurations often result in unwanted frictions/singularities as well as non-intuitive feels. To overcome problems associated with serial/parallel mechanisms, several different versions of ball-joint-like spherical motors [8–16] have been proposed. These ball-joint-like devices, which offer singularity-free (except at the boundary) smooth multi-DOF motion in one joint, have significant potentials in haptic applications. Fig. 1 shows a permanent magnet spherical motor (PMSM) [17] consisting of a stator on which the rotor is concentrically supported through a ball-joint bearing. The stator and rotor, respectively, house N_s electromagnets (EMs) and N_r permanent magnets (PMs). As currents flow through the EMs, a three-dimensional (3D) torque can be generated providing "haptic feel" to the human user. When maneuvering the PMSM haptic device, the operator's orientation input is translated into motion commands upon which the

---

* Corresponding author at: Woodruff School of Mechanical Engineering, Georgia Institute of Technology, Atlanta, GA 30332, USA. Tel.: +1 404 894 7402; fax: +1 404 894 9342.

E-mail addresses: kbai@gatech.edu (K. Bai), jijingjing@zju.edu.cn (J. Ji), kokmeng.lee@me.gatech.edu (K.-M. Lee), zsy@zju.edu.cn (S. Zhang).
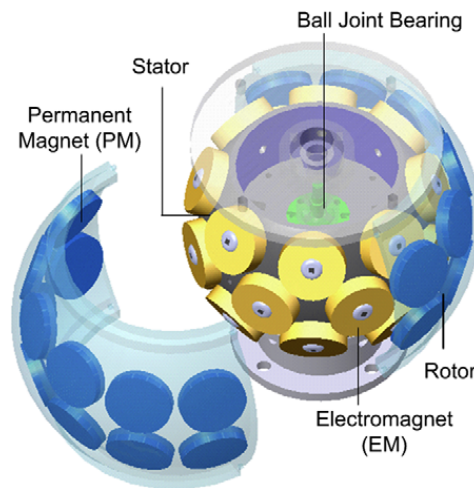
Fig. 1. CAD model of a spherical motor [17].

simulated force/torque vector is calculated in a virtual environment and applied on the rotor enabling the user to have a realistic experience. This computational sequence requires simultaneously measuring the rotor orientation and computing the torque coefficient vectors (TCVs) which relate the current inputs to the applied torque of the PMSM in real time.

Traditional rotor orientation measurements of a ball-joint-like device rely on multiple single-axis encoders [8] requiring an external mechanism to mechanically decouple the motion into three independent directions. The motion-constraining mechanism introduces additional inertia and friction; the former limits the bandwidth of the haptic device while the latter is a primary cause of physical wear and tear. To overcome these problems, several different designs of non-contact orientation sensors have been developed, which include optical [18] and vision-based sensors [19] and more recently direct methods utilizing the magnetic-field measurements of the moving rotor PMs [20]. As compared to its other noncontact counterparts for a dexterous PMSM haptic device, magnetic sensors do not require "a line of sight" and permit sensing across multiple non-ferromagnetic mediums. Magnetic field-based methods offer a fast and non-contact solution for orientation detection and have the advantage of invariant to environmental factors (temperature, light, etc.).

Unlike a serial/parallel mechanism using single-axis actuators and sensors, the PMSM-based haptic device has more current inputs through the EMs than its output (mechanical DOF). For three-DOF, the number of EM currents (or N_s) is greater than three, and thus an optimal input vector that minimize the energy consumed for a specified torque can be found. Traditional solutions to current optimization of a PMSM require explicit orientation measurements in real time prior to computing the TCVs using an orientation-based model [10,13–15]. This sequential computation compromises sampling rate and results in error accumulation. Since both the magnetic field and the output torque are functions of rotor orientation, the orientation and TCVs can be simultaneously computed in parallel once the magnetic field measurements are available; this novel scheme greatly improves the sampling rate and reduces error accumulation.

Snap-fits are widely used in various types of products, equipment and power systems to provide attachment functionality in assemblies as they can be incorporated as feature molded in parts thus reducing part count; and their ease of assembly and disassembly lowers manufacturing cost and time. A performance analysis of snap-fits requires not only virtual simulation but also a good understanding of the inherently motion/force transmission through deformation encountered during assembly and disassembly, in which a sense of human touch to feel the level of contact force is needed. Ref. [4] investigated the parametric effects (which include material properties, hook shape and shear deformation) on the force/deflection relationship governing the assembly/disassembly processes of a snap-fit. This study has provided a basis for developing embedded algebraic solutions to achieve realistic force feedback with the aid of commercial PHANTOM haptic device. However, as manual snap-fit motion is essentially a multi-DOF motion (due to the fact that human feeling is generally qualitative or quantitatively less precise), this early work [4] assumes that the assembly/disassembly of a snap-fit ideally undergoes one-DOF motion consequently and neglects other "uncontrollable" human-based motion factors. For this reason, we take into accounts in this paper some unintended coupling displacement/rotation motions commonly encountered in manual snap-fits. As will be demonstrated, the ball-joint-like spherical device (such as a PMSM) offers an intuitive haptic feeling than a traditional serial/parallel mechanism. It is expected that the generalized PMSM-based haptic evaluation can be extended for assembly of other products.

The remainder of this paper offers the following:

– A PMSM haptic device, which offers a smooth motion command decoupling the 6-DOF into two configuration (translational and rotational) modes, is presented. The force/torque feedback from the virtual environment can be rendered on the PMSM by supplying currents through the EMs to generate a torque on the rotor. The motion command and force/torque feedback representations are defined in each mode. Unlike commercial multi-DOF manipulators, a direct mapping capitalizing the existing field is used to compute the magnetic torque and provide the required force/torque feedback without explicit orientation measurements in real-time.
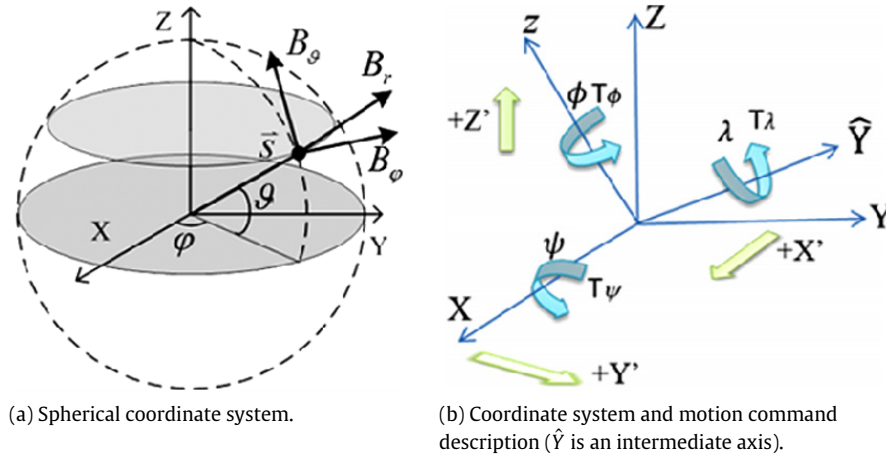
(a) Spherical coordinate system.

(b) Coordinate system and motion command description ($\hat{Y}$ is an intermediate axis).

Fig. 2. Illustration of position and torque commands.

– The PMSM haptic device has been implemented as an interface between a human user and the virtual design environment for a snap-fit disassembly. The analyses considered in this paper extend the study in [4] to account for the unintended displacement/rotation due to imprecise human motions during disassembly of a snap-fit with the aid of multi-DOF PMSM haptic device. The disassembly process is realistically simulated such that the designer can appropriately adjust the displacement and rotate angle during disassembly in a virtual environment.

2. Description of the PMSM haptic device

In Fig. 1, the radial magnetization axes (of both the PMs and the air-cored EMs) point towards the joint center; and the entire structure (except for the PMs) is non-magnetic. In spherical coordinates (ϑ, ϕ, r), the magnetization axes can be characterized by a vector pointing from the origin to the centroid of each PM or EM as shown in Fig. 2(a). The complete description of PM and EM positions is given in Appendix A. Fig. 2(b) illustrates the coordinate systems of a PMSM, where XYZ is the stator frame (stationary); *xyz* is the rotor frame; and **q** is a vector of XYZ Euler angles describing the rotor orientation:

$$\mathbf{q} = \begin{bmatrix} \psi & \lambda & \phi \end{bmatrix}^T. \tag{1}$$

In design and control of a PMSM, both the forward and inverse torque models are needed. The former (used in design analysis) computes the three torque components for a specified set of electrical currents. Unlike the forward model where the solutions are unique, there are infinite solutions to the inverse torque model (that is required in real-time control) as the number of current inputs is more than three (the number of desired DOF or torque constraint equations). With linear magnetic properties, the electromagnetic torque of the PMSM has the form [10]:

$$\mathbf{T} = \begin{bmatrix} T_\psi & T_\lambda & T_\phi \end{bmatrix}^T = [\mathbf{K}]\,\mathbf{u} \tag{2}$$

where

$$[\mathbf{K}] = [\mathbf{K}_1 \quad \cdots \quad \mathbf{K}_j \quad \cdots \quad \mathbf{K}_{Ns}]; \tag{3a}$$

$$\mathbf{u} = [i_1 \quad \cdots \quad i_j \quad \cdots \quad i_{Ns}]^T; \tag{3b}$$

i_j is the current input to EM_j. In (3a), $\mathbf{K}_j$ is the torque coefficient vector (TCV) of EM_j where the TCV is the resultant torque acting on the rotor due to a 1-A current flowing through a single EM. An optimal current vector minimizing the total input energy can be found using Lagrange multipliers [21]:

$$\mathbf{u} = [\mathbf{K}]^T ([\mathbf{K}][\mathbf{K}]^T)^{-1}\mathbf{T}. \tag{4}$$

Eqs. (2) and (4) are the forward and inverse torque models of the PMSM.

For computing the orientation and TCV, a set of magnetic sensors (given in Appendix A) measuring the magnetic flux density **B** is installed on the stator with their sensor axes pointing in the (ϑ, φ, r) directions for measuring the three components $(B_\varphi, B_\vartheta, B_r)$.

2.1. Two-mode configuration design for 6-DOF manipulation

Physically, the PMSM has three-DOF of rotational motion but can be configured to operate in two modes to achieve two independent sets of (rotational and translational) motion in the target space (as shown in Fig. 2(b)):

– *Rotational mode*: The PMSM can be directly used as an integrated rotational motion-sensor and torque-actuator. The three-DOF rotational motions are defined as:

$$\begin{bmatrix} \lambda' & \psi' & \phi' \end{bmatrix}^T = \begin{bmatrix} \varsigma_1\lambda & \varsigma_2\psi & \varsigma_3\phi \end{bmatrix}^T \tag{5a}$$

where the constants, ζ_1, ζ_2 and ζ_3, can be tuned to meet specific needs; and the prime denotes the coordinates in virtual environment (similarly hereinafter). Similarly, the PMSM can simulate *physically* the torque feedback from the *virtual* target by directly applying Lorenz torques on its rotor in real time enabling the user to have the haptic feel. The three torque components have the form (with constant η_1, η_2 and η_3):

$$\begin{bmatrix} T_\psi & T_\lambda & T_\phi \end{bmatrix}^T = \begin{bmatrix} \eta_1 T_{\psi'} & \eta_2 T_{\lambda'} & \eta_3 T_{\phi'} \end{bmatrix}^T . \tag{5b}$$

– *Translational mode*: The PMSM can also be configured in translational domain such that the user's rotational motion on the rotor is interpreted into translational displacements. By the same token, the force feedback from the virtual target is actuated as torques on the rotor enabling the user to have an equivalent haptic experience:

$$\begin{bmatrix} X' & Y' & Z' \end{bmatrix}^T = \begin{bmatrix} \hat{\varsigma}_1\lambda & \hat{\varsigma}_2\psi & \hat{\varsigma}_3\phi \end{bmatrix}^T \tag{6a}$$

$$\begin{bmatrix} T_\psi & T_\lambda & T_\phi \end{bmatrix}^T = \begin{bmatrix} \hat{\eta}_1 F_{Y'} & \hat{\eta}_2 F_{X'} & \hat{\eta}_3 F_{Z'} \end{bmatrix}^T \tag{6b}$$

where $\hat{\varsigma}_1$, $\hat{\varsigma}_2$, $\hat{\varsigma}_3$ and $\hat{\eta}_1$, $\hat{\eta}_2$, $\hat{\eta}_3$ are constants.

By switching between these two modes, the PMSM is capable of two independent sets of three-DOF motions in the target space providing sensible force/torque feedback to the user in real time.

2.2. Numerical model for magnetic field/torque computation

As a physical EM or PM (that is axially magnetized and has a cylindrical shape of radius a and length l) can be mathematically modeled as a distributed set of dipoles (referred to here as a DMP [22] model), the magnetic flux density as well as the magnetic force/torque can be then computed in close-forms [17]. The dipole (with strength m) is defined here as a pair of source and sink separated by a distance l. This model for an axially magnetized cylindrical PM or EM consists of k circular uniformly spaced loops of n equally spaced dipoles parallel to the magnetization vector:

$$\bar{a}_j = a_o j/(k+1) \quad \text{at } z = \pm\bar{\ell}/2 \quad (0 \le j \le k). \tag{7}$$

The flux density generated by a PM or EM at a point in space can be computed using (8):

$$\mathbf{B} = \frac{\mu_0}{4\pi} \sum_{i=0}^{k} m_i \sum_{j=1}^{n} \left(\frac{\mathbf{R}_{ij+}}{\left|\mathbf{R}_{ij+}\right|^3} - \frac{\mathbf{R}_{ij-}}{\left|\mathbf{R}_{ij-}\right|^3} \right) \tag{8}$$

where $\mathbf{R}_{ij+}$ and $\mathbf{R}_{ij-}$ are the vectors from the source and sink of the jth dipole on the ith loop to the point being considered, respectively; and m_i is the pole strength of the poles on ith loop.

Given that each of the EM (or PM) is characterized by n_s (or n_r) dipoles, the component $\mathbf{K}_j$ of the EM_j can be derived using the dipole force method [17]:

$$\mathbf{K}_j = \frac{\mu_0}{4\pi} \sum_{i=1}^{N_r \times n_r} m_{r_i} \sum_{p=1}^{n_s} m_{s_p} (\mathbf{R}_{r_{i+}s_{p+}} - \mathbf{R}_{r_{i+}s_{p-}}) \times \mathbf{R}_{r_{i+}} - (\mathbf{R}_{r_{i-}s_{p+}} + \mathbf{R}_{r_{i-}s_{p-}}) \times \mathbf{R}_{r_{i-}}. \tag{9}$$

In Eq. (9), $\mathbf{R}_{r_{i\pm}s_{p\pm}} = (\mathbf{R}_{r_{i\pm}} - \mathbf{R}_{s_{p\pm}})/\left|\mathbf{R}_{r_{i\pm}} - \mathbf{R}_{s_{p\pm}}\right|^3$ where $\mathbf{R}_{r_{i\pm}}$ ($\mathbf{R}_{s_{p\pm}}$) is the ith (pth) pole location of the rotor (EM_j); and the signs, $(+)$ and $(-)$, stand for the source and the sink of the dipole respectively; and m_{ri} (m_{sp}) are the pole strength of the ith (pth) dipole pair in the rotor (EM_j).

2.3. Field-based TCV estimation

As shown in (8), the magnetic fields of the PMs and hence the TCV of the EMs in (9) depend on the rotor orientation. Computing the TCV using orientation-based models would result in significantly long sampling time as the orientation and TCV must be sequentially computed. It is desired that the TCV can be derived directly from magnetic field measurements; the relationship between them can be characterized with a direct mapping as illustrated in Fig. 3 where an artificial neural network (ANN) is used to model the complex relationship between the magnetic field and the TCV through the Levenberg–Marquardt supervised back-propagation training algorithm.

As an illustration, consider the TCV ($\mathbf{K}_{17}$) of EM_{17} (located on the X axis); note that the indexing of the sensors and EMs can be found in Appendix A. The magnetic flux densities as well as the TCV are computed with (8) and (9) in the working space of the PMSM described as

$$-22.5° \le (\psi, \lambda) \le 22.5°, \qquad 0° \le \phi < 360°.$$

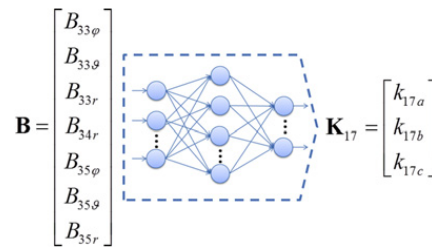$$\mathbf{B} = \begin{bmatrix} B_{33\varphi} \\ B_{33\vartheta} \\ B_{33r} \\ B_{34r} \\ B_{35\varphi} \\ B_{35\vartheta} \\ B_{35r} \end{bmatrix} \qquad \mathbf{K}_{17} = \begin{bmatrix} k_{17a} \\ k_{17b} \\ k_{17c} \end{bmatrix}$$

Fig. 3. ANN parameters.
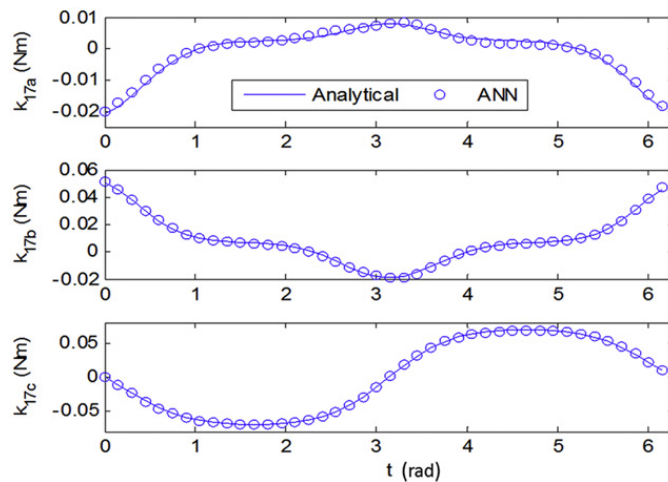
Fig. 4. Analytical and ANN-estimated results.

Table 1
DMP parameters.

PM	EM
$a = 15.875$ mm, $l = 0.2$, $\mu_o M_o = 1.31$ T	$a = 15.88$ mm, $a_r = 0.3$, $l = 0.3$, # of turns = 1000
$\text{DMP}_{PM} : n = 10$, $k = 4\bar{l}/l = 0.3$	$\text{DMP}_{EM} : n = 16$, $k = 6$, $\bar{l}/l = 0.442$
m_j (μA/m): 33.5, 24.5, 57.6, 52.0, 276.1	m_j(μA/m): 1.476, 0.547, 1.618, 1.644, 1.654, 1.325, 0.592

The parameters used for the computations are described in Table 1. An ANN (with 1 hidden layer and 10 nodes) was trained with the computed data (16200 samples). The inputs, outputs as well as the ANN parameters are shown in Fig. 3. As an illustrative comparison, the components of $\mathbf{K}_{17}$ are estimated with the ANN and the $\mathbf{B}$ computed using (8) while the rotor follows a trajectory given by

$$\psi = 10° \sin t, \qquad \lambda = 5° \sin t, \qquad \phi = 5°, \quad t \in [0, 2\pi].$$

The computed results agree excellently well with the analytical solutions computed using (9) along the trajectory as compared in Fig. 4.

3. Snap-fit simulation

Snap-fits offer resistance to engagement during assembly and disassembly in various types of products, equipment, and power systems. A means to experience the force/torque feedback is desirable for manual assembly in many applications particularly for snap-fit engagement of critical components. Of particular interest here is to explore the application of a PMSM as a haptic device for experiencing the snap-fit assembly/disassembly processes in a virtual environment, and enabling a designer to qualitatively evaluate the level of deformation through realistic force/torque feedback.

Fig. 5(a) shows a typical haptic evaluation procedure during the design optimization of a product. Often, several optional configurations for a product are designed considering tradeoffs among many parametric effects (including both geometric construction and material properties). As illustrated in the dashed box labeled as "Optimization", these design configurations are presented in the parameter vector $\mathbf{P}$ and output to the "design forward model" along with the vector $\mathbf{X}$ containing the sensed positional and/or orientation motion corresponding to the human input $\mathbf{X_h}$ manipulated by a human designer on the PMSM haptic device. Through the "design forward model", the multi-DOF (manual assembly or disassembly) force/torque vector $\mathbf{F}$ is then solved in terms of the sensed motion $\mathbf{X}$ (that is translated into motion command driving the assembly/disassembly component in virtual space). Since PMSM is a 3-DOF angular device, the "model transformation"
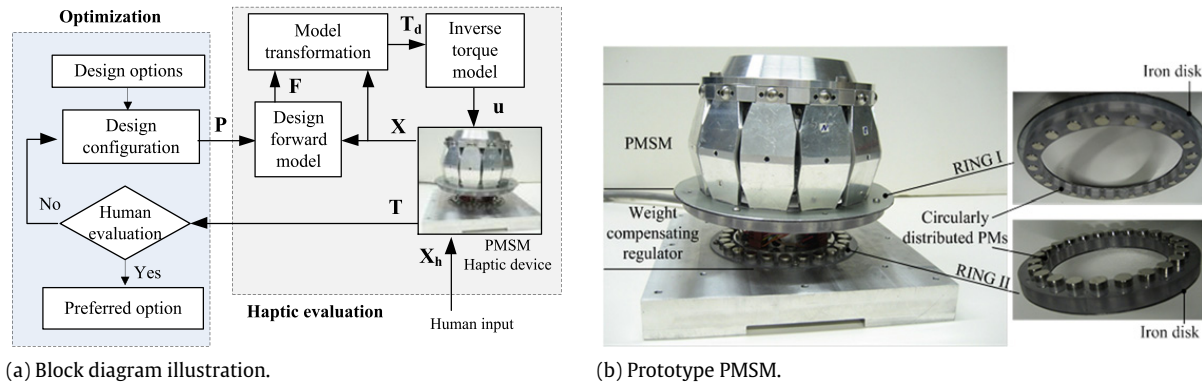
(a) Block diagram illustration.

(b) Prototype PMSM.

Fig. 5. Haptic evaluation procedure and prototype PMSM.

Table 2
Current input configuration of the EMs.

$i_1 = i_{13} = u_1$	$i_5 = i_9 = u_5$	$i_{17} = i_{21} = u_9$
$i_2 = i_{14} = u_2$	$i_6 = i_{10} = u_6$	$i_{18} = i_{22} = u_{10}$
$i_3 = i_{15} = u_3$	$i_7 = i_{11} = u_7$	$i_{19} = i_{23} = u_{11}$
$i_4 = i_{16} = u_4$	$i_8 = i_{12} = u_8$	$i_{20} = i_{24} = u_{12}$

converts the required force/torque $\mathbf{F}$ and sensed motion $\mathbf{X}$ into the desired torque vector $\mathbf{T}_d$ for computing an optimal set of current inputs using the inverse torque model (4) to drive the spherical rotor. From the magnetic field measurements both the rotor orientation [20] and the TCVs can be determined directly using ANNs, upon which an optimal set of current inputs $\mathbf{u}$ can be computed. The current inputs (flowing into the EMs in the presence of the rotor PM field) result in feedback torque $\mathbf{T}$ acting on the rotor while the designer maneuvers the PMSM haptic device. Thus, the designer can then select a preferred configuration based on the "feel" by evaluating the product performance in a virtual environment.

Since the rotor of the PMSM is essentially an inverted pendulum and becomes inherently unstable when no current inputs are supplied, a weight-compensating regulator (WCR) is incorporated in the prototype PMSM as shown in Fig. 5(b). The WCR consisting of two circular PM rings uses a couple of distributed repulsive PM forces to support the rotor angularly against gravity and tends to maintain the rotor at its equilibrium and effectively reduces the input electrical energy required (and thus heat generation). The restoring torque of the WCR (as a function of the inclination angle) can be compensated when generating the torque feedback. Due to the rotor symmetrical PM configuration, the EMs are grouped into 12 electrical inputs (as described in Table 2) with each group of two EMs (symmetrical about the motor center) connected in series.

3.1. Snap-fit performance analyses

Fig. 6 illustrates the snap-fit assembly of a typical cantilever hook [4] (base thickness h_o, width w and length l_t) with a wedge-shaped end characterized by the height h_b and angles (α, β). In Fig. 6, the shaded cantilever indicates its initial state; and δ is the beam deflection as the matching part contacts the wedge at x. As the matching part advances (or retracts) for assembly (or disassembly), the contact point slides along the front (or rear) surface of the wedge as well as deflects the beam. To offer intuitive insights and facilitate design, we normalize the forces to (Ewh_o) and geometrical dimensions to h_o as follows:

$$\begin{bmatrix} F_x \\ F_y \end{bmatrix} = \frac{1}{Ewh_o} \begin{bmatrix} f_x \\ f_y \end{bmatrix}; \qquad X = \frac{x}{h_o}; \qquad L_b = \frac{\ell_b}{h_o}; \qquad H_b = \frac{h_b}{h_o}; \qquad L_t = \frac{\ell_t}{h_o}.$$

The normalized beam deflection $\Delta = \delta/h_o$ can be expressed as a mechanical impedance Ω, where the subscripts "+" and "−" indicate the deflections are in the $+y$ and $-y$ directions respectively

$$\Omega = \Delta/F_y = \Omega_+ + s\left(f_x/f_y\right)\Omega_-$$

$$\text{where } s = \begin{cases} +1, & \text{for } x = [\ell_b, \ell_m) \\ -1, & \text{for } x = (\ell_m, \ell_t] \end{cases} \text{ and at } x = \ell_m \ s = \begin{cases} -1 & \text{assembly} \\ +1 & \text{disassembly}. \end{cases} \tag{10}$$

The assembly force f_x and deflecting force f_y are related by (11), where μ is the friction coefficient between the two sliding surfaces:

$$\frac{f_x}{f_y} = \begin{cases} \tan(\gamma' + \tan^{-1}\mu) & \text{Insertion} \\ \mu & \text{Dwelling} \\ \tan(\gamma' - \tan^{-1}\mu) & \text{Retention} \end{cases} \quad \text{where } \gamma' = \begin{cases} \alpha' = \alpha + \tan^{-1}(\delta/x), & \text{for } x = [\ell_m, \ell_t]; \\ \beta' = \beta - \tan^{-1}(\delta/x), & \text{for } x = [\ell_b, \ell_m]. \end{cases} \tag{11}$$
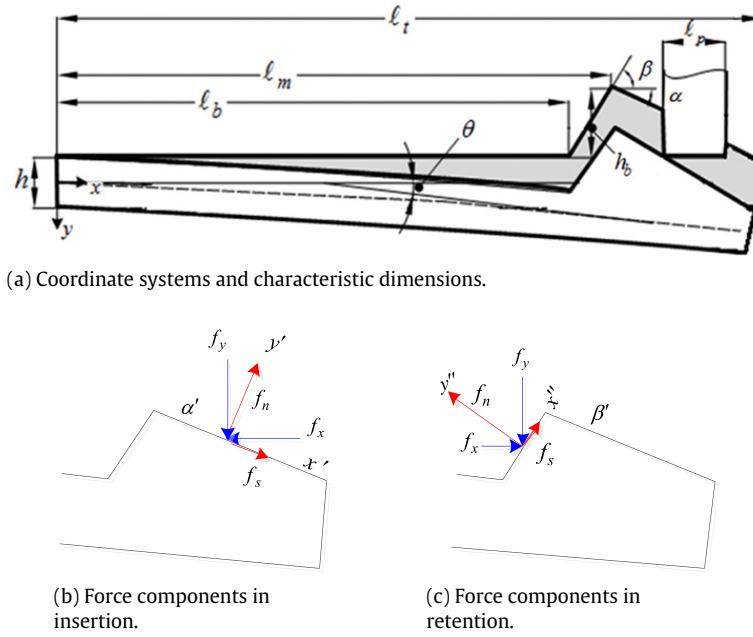
(a) Coordinate systems and characteristic dimensions.

(b) Force components in insertion.

(c) Force components in retention.

Fig. 6. Cantilever hook and matching part.

(a) CAD model.

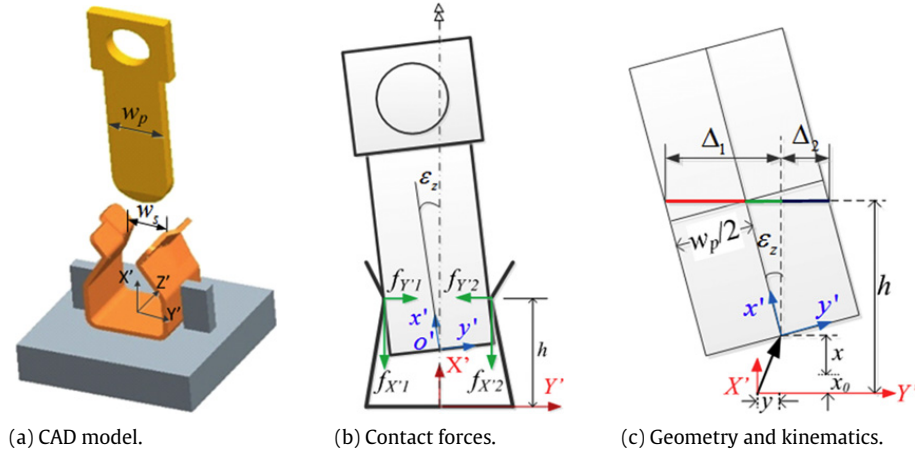(b) Contact forces.

(c) Geometry and kinematics.

Fig. 7. Schematics illustrating the disassembly, where $x_0 = (w_p/2) \sin(\varepsilon_z)$ in Fig. 7(c).

The normalized deflection $(\Delta_+ = \delta_+/h)$ is a function of F_y and can be expressed as

$$\Omega_+ = \frac{\Delta_+}{F_y} = \sum_{i=1}^{3} \Omega_{i+} = 4KL_b^3 + \int_{\ell_b}^{x} \frac{12x^2 dx}{h^3(x)} + \frac{pE}{G} \int_{\ell_b}^{x} \frac{dx}{h(x)} \quad \text{where } K = 1 + \frac{0.3}{L_b^2}\left(\frac{E}{G}\right) \tag{12}$$

$$\text{where } h(x) = \begin{cases} h_o, & \text{for } x = [0, \ell_b] \\ h_o + (x - \ell_b)\tan\beta, & \text{for } x = [\ell_b, \ell_m]; \ \beta = [0, \pi/2] \\ h_o + (\ell_t - x)\tan\alpha, & \text{for } x = [\ell_m, \ell_t]; \ \alpha = [0, \pi/2] \end{cases}$$

and $h(x) = h_o + h_b$ when $\alpha = \pi/2$ or $\beta = \pi/2$.

Similarly, the normalized deflection $(\Delta_- = \delta_-/h_o)$ is a function of F_x:

$$\Omega_- = \frac{\Delta_-}{sF_x} = \Omega_{1-} + \Omega_{2-} = 6X\left(\frac{h(x)}{h_o} - \frac{1}{2}\right)L_b + 6X\left(\frac{h(x)}{h_o} - \frac{1}{2}\right)\int_{\ell_b}^{x} \frac{h_o^2 dx}{h^3(x)}. \tag{13}$$

3.2. Snap-fit haptic application

Fig. 7(a) shows the CAD model of an "outlet" (commonly in household products) demonstrating the contact feeling of a typical cantilever snap-fit during design. The outlet snap-fit consists of a cold-drawn brass plug and a fixed socket made of rolled phosphor bronze. The extraction of the plug from the socket undergoes the dwelling process of the snap fit as illustrated in Fig. 7(b).

Table 3
Simulation parameters.

Parameter	Design configuration [4]
Socket (mm)	$\ell_b = 5.4$, $\ell_m = 9.6$, $\beta = 58.8°$, $h_b = 1.8$, $h_o = 0.6$, $w = 8$, $w_s = 4.8$ Young's modulus $E = 1.13$ GPa; Poisson's ratio $\upsilon = 0.41$
Plug (mm)	$w_p = 6.3$, thickness $= 1.5$ $E = 0.93$ GPa and $\upsilon = 0.35$
μ (friction coefficient)	0.134
Coef. in 3rd term of Eq. (12)	$p = 6/5$

The disassembly of the outlet snap-fit can be considered as a nonlinear beam deflection problem with the movement of the plug as an input. Since the plug-width is larger than the distance of the initial socket opening, this difference leads to the beam deflection δ. As shown in Fig. 7(b), the detaching motion of the plug can be characterized as a translation in X direction and rotation about Z axis (ε_z). The forces applied on the plug can be computed as illustrated in Fig. 7(b) where the net forces ($F_{X'}$, $F_{Y'}$) due to the contact forces are given by (14):

$$\begin{bmatrix} F_{X'} \\ F_{Y'} \end{bmatrix} = \begin{bmatrix} f_{X'1} + f_{X'2} \\ f_{Y'1} - f_{Y'2} \end{bmatrix}. \tag{14}$$

Since the extraction undergoes a dwelling process; thus Eqs. (10) and (11) apply with $s = +1$ and $fx/fy = \mu$:

$$\begin{bmatrix} f_{X'1} \\ f_{X'2} \end{bmatrix} = \frac{\mu E w}{\Omega_+ + \mu \Omega_-} \begin{bmatrix} \Delta_1 - w_s/2 - y \\ \Delta_2 - w_s/2 + y \end{bmatrix} \quad \text{and} \tag{15a}$$

$$\begin{bmatrix} f_{Y'1} \\ f_{Y'2} \end{bmatrix} = \frac{1}{\mu} \begin{bmatrix} f_{X'1} \\ f_{X'2} \end{bmatrix}. \tag{15b}$$

In this illustrative example, the plug is initially inserted such that $\varepsilon_z = 0$ (and $x'y'$ coincides with $X'Y'$). The kinematic parameters can be derived with the aid of Fig. 7(c):

$$\Delta_{1,2} = \frac{w_p}{2 \cos \varepsilon_z} \pm (h - x - x_o) \tan \varepsilon_z. \tag{16}$$

Hence, the net forces can be written in closed form given by (17) where Ω_+ and Ω_- are given in Appendix B:

$$\begin{bmatrix} F_{X'} \\ F_{Y'} \\ F_{Z'} \end{bmatrix} = \frac{E w}{\Omega_+ + \mu \Omega_-} \begin{bmatrix} \mu w_p \sec \varepsilon_z - \mu w_s \\ 2 \tan \varepsilon_z (h - x_0 - x) - 2y \\ 0 \end{bmatrix}. \tag{17}$$

Similarly, the net torque about o' is:

$$\begin{bmatrix} T_{X'} \\ T_{Y'} \\ T_{Z'} \end{bmatrix} = \begin{bmatrix} 0 \\ 0 \\ F_{Y'} (h - x - x_0) \end{bmatrix} = \begin{bmatrix} 0 \\ 0 \\ 2 \tan \varepsilon_z (h - x - x_0)^2 - 2y (h - x - x_0) \end{bmatrix}. \tag{18}$$

Ideally, the initial tilting angle during disassembly equals to zero and hence the reaction forces along the Y axis cancel out. However, if the tilting angle is not zero, an unbalanced reaction force will result and will be felt by the operator through the feedback of the PMSM. As an illustration, a two-phase disassembly process is simulated with values of the simulation parameters given in Table 3. The simulated results are discussed as follows:

Phase 1: The plug is initially tilted with $\varepsilon_z = 2°$ and then pulled out along the X' axis. The PMSM is in translational mode. The interaction between the PMSM and the snap-fit assembly as well as the motion command and the force feedback are described in row B of Fig. 8(a). The results (as shown in row A of Fig. 8(b)) indicate that $F_{X'}$ is constant and the non-zero $F_{Y'}$ implies that the plug deviates from the X' axis.

Due to the initially tilted position, the process starts at x_0 with $y = 0$ throughout the simulation. The force feedback is translated into desired torques so that the current inputs can be computed using the inverse torque model where the TCVs are derived using the trained ANN directly from the magnetic fields. For clarification, the current inputs are group into two plots realizing T_ψ (due to $F_{X'}$) and T_λ (due to $F_{Y'}$) as shown in the bottom row of Fig. 8(a). The resultant torque perceived by a human operator through the rotor can be obtained by summing both sets of currents and inputting them into the EMs.

Phase 2: The tilting angle is adjusted by the rotational mode of the PMSM. The interaction leading to the motion command and the force feedback along with the unbalanced reaction torque are described in Fig. 8(b). As shown in the top row of Fig. 8(b), the torque decreases as the tilting angle increases and becomes zero when the tilting angle approaches zero. The torque feedback in this process can be realized with the current inputs contributing the desired torque shown in the bottom row of Fig. 8(b). After the tilting angle is adjusted, the PMSM will be switched to translational mode while the disassembly motion proceeds.
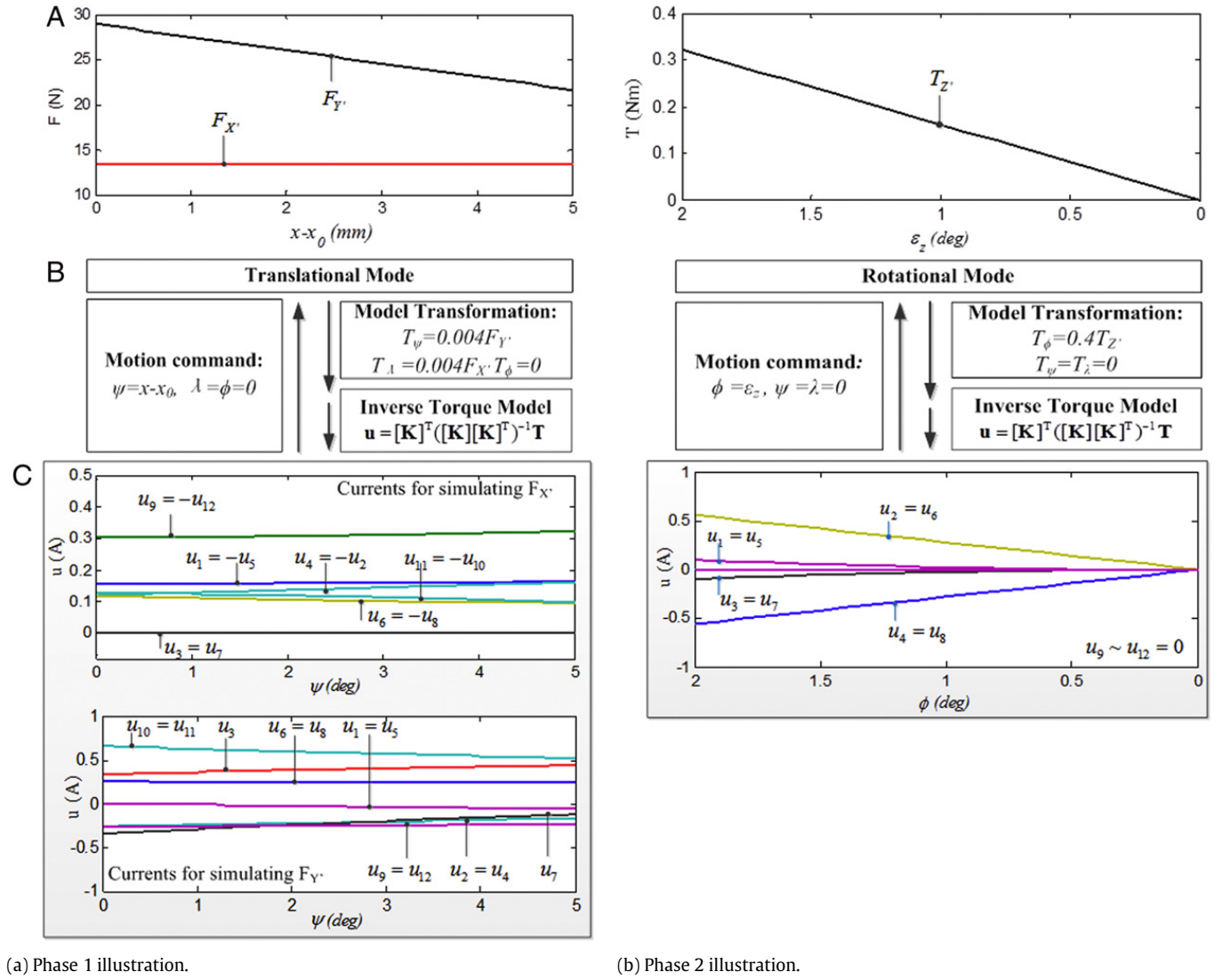
(a) Phase 1 illustration.　　　　　　　　　　　　　　　　(b) Phase 2 illustration.

Fig. 8. Simulation responses.

4. Conclusion

A two-mode PMSM capable of providing smooth, continuous multi-DOF motion is presented in the context of a haptic application. With the two-mode configuration, the PMSM can offer 6-DOF motion commands for manipulating a target in a virtual computer-aided engineering environment while providing sensible force/torque feedback for human operators. A field-based TCV estimation method using ANN is introduced, which estimates the TCV directly from magnetic fields and permits parallel processing in current input computation. The PMSM haptic device has been numerically demonstrated as an interface between the designer and the virtual design environment for a snap-fit disassembly process. The two-DOF snap-fit haptic applications show that the PMSM offers the human operator an effective means to manipulate targets with multi-DOF force/torque feedback in real time, which greatly improves the performance of such manually operated tasks.

Acknowledgment

Appendix A. PM/EM/sensor position coordinates

The magnetization axes of the PMs or EMs can be characterized by a vector pointing from the origin to the centroid of each PM and EM. The adjacent PMs have alternating magnetization axis. The centroids as well as the sensor positioning are defined in terms of spherical coordinates (as shown in Fig. 2(a) in rotor frame (for PMs) and stator frame (for EMs and sensors) respectively, which have the following form

$$\vec{r}_j = R \left[C_{\varphi_j} S_{\vartheta_j} \quad S_{\varphi_j} S_{\vartheta_j} \quad C_{\vartheta_j} \right]^T . \tag{A.1}$$

Table A.1
Locations of PMs, EMs and sensors.

j	Sensor (in XYZ)			EM (in XYZ)			PM (in xyz)	
	1–16	17–32	33–48	1–8	9–16	17–24	1–12	13–24
ϑ (°)	−26	26	0	−26	26	0	−15	15
φ (°)	$22.5(j-1)$	$22.5(j-17)$	$22.5(j-33)$	$45(j-1)$	$45(j-9)+22.5$	$45(j-17)+22.5$	$30(j-1)$	$30(j-13)$

$R_{PM} = 67.9$ mm, $R_{EM} = 56.8$ mm, $R_{Sensor} = 62.4$ mm.

The parameters are given in Table A.1.

Appendix B. Equations for computing reaction forces

$$\Omega_+ = \sum_{i=1}^{3} \Omega_{i+} \quad \text{and} \quad \Omega_- = \sum_{j=1}^{2} \Omega_{j-} \tag{B.1}$$

$$\rho(h_o) = \frac{1}{1+H_b}; \tag{B.2a}$$

$$H_x = 1 + \frac{\delta}{h_o}; \tag{B.2b}$$

$$\frac{E}{G} = 2.6 \tag{B.2c}$$

$$\Omega_{1+} = 4\left[1 + \frac{0.3}{L_b^2}\left(\frac{E}{G}\right)\right] L_b^3 \tag{B.3}$$

$$\Omega_{2+} = \frac{6}{\tan^3 \sigma}\left[-2\ln\rho(h_o) - 4H_b\rho(h_o)\left(1 - L_b\tan\sigma\right) + H_b\left(2 + H_b\right)\left(1 - L_b\tan\sigma\right)^2 \rho^2(h_o)\right] \tag{B.4}$$

$$\Omega_{3+} = -\frac{kE}{G}\frac{\ln\rho(h_o)}{\tan\sigma}, \tag{B.5a}$$

$$\Omega_{1-} = 3L_m\left(2H_x + 1\right)L_b, \tag{B.5b}$$

$$\Omega_{2-} = \frac{3L_m}{2\tan\sigma}\left(2H_x + 1\right)\left[1 - \rho^2(h_o)\right]. \tag{B.5c}$$

References

[1] C. Moore, M. Peshkin, J. Colgate, Cobot implementation of virtual paths and 3-D virtual surfaces, IEEE Trans. Robot. Autom. 19 (2003) 347–351.
[2] R. Ellis, O. Ismaeil, M. Lipsett, Design and evaluation of a high performance haptic interface, Robotica 4 (1996) 321–327.
[3] Z.Y. Yang, L.L. Lian, Y.H. Chen, Haptic function evaluation of multi-material part design, Comput.-Aided Des. 37 (2005) 727–736.
[4] J.J. Ji, K.-M. Lee, Y.S. Zhang, Cantilever snap-fit performance analysis for haptic evaluation, ASME J. Mech. Des. 133 (2011) 121004(1–8).
[5] D. Ryu, C. Cho, M. Kim, J. Song, Kinematic analysis and design of a 6 DOF haptic master for teleportation of a mobile manipulator, in: IEEE/RSJ Int. Conf. on Intelligent Robots and Systems, 2003, pp. 2235–2240.
[6] J. Yoon, J. Ryu, Design, fabrication and evaluation of a new haptic device using a parallel mechanism, IEEE/ASME Trans. Mechatronics 6 (2001) 211–233.
[7] J. Arata, H. Kondo, N. Ikedo, H. Fujimoto, Haptic device using a newly developed redundant parallel mechanism, IEEE Trans. Robot. 27 (2011) 201–214.
[8] G. Vachtsevanos, K. Davey, K.-M. Lee, On the development of a novel intelligent robotic manipulator, IEEE Control Syst. Mag. 3 (1987) 9–15.
[9] A. Foggia, E. Oliver, F. Chappuis, New three degrees of freedom electromagnetic actuator, in: IAS Annual Meeting, 1988.
[10] K.-M. Lee, R.B. Roth, Z. Zhou, Dynamic modeling and control of a ball-joint-like variable-reluctance spherical motor, ASME, J. Dyn. Syst. Meas. Control 118 (1996) 29–40.
[11] J. Wang, G. Jewel, D. Howe, Analysis, design and control of a novel spherical permanent magnet actuator, IEEE Proc. Electr. Power Appl. 145 (1998) 61–71.
[12] M. Week, T. Reinartz, G. Henneberger, R.W.D. Doncker, Design of a spherical motor with three degrees of freedom, CIRP Ann. 49 (2000) 289–294.
[13] G.S. Chirikjian, D. Stein, Kinematic design and commutation of a spherical stepper motor, IEEE/ASME Trans. Mechatronics 4 (1999) 342–353.
[14] L. Yan, I. Chen, C. Lim, G. Yang, W. Lin, K.M. Lee, Design and analysis of a permanent magnet spherical actuator, in: IEEE/RSJ Int. Conf. on Intelligent Robots and Systems, 2005, pp. 2607–2612.
[15] H. Son, K. Bai, J. Lim, K.-M. Lee, Design of multi-DOF electromagnetic actuators using distributed multipole models and image method, Int. J. Appl. Electromagn. Mech. 34 (2010) 195–210.
[16] K. Bai, K.-M. Lee, S. Foong, Direct field-feedback control for multi-DOF spherical actuators, in: IEEE Int. Conf. on Robotics and Automation, ICRA, 2011, pp. 5825–5830.
[17] K.-M. Lee, K. Bai, J. Lim, Dipole models for forward/inverse torque computation of a spherical motor, IEEE/ASME Trans. Mechatronics 14 (2009) 46–54.
[18] K.-M. Lee, D. Zhou, A real-time optical sensor for simultaneous measurement of three-DOF motions, IEEE/ASME Trans. Mechatronics 9 (2004) 499–507.
[19] H. Garner, M. Klement, K.-M. Lee, Design and analysis of an absolute non-contact orientation sensor for wrist motion control, in: Proceedings of IEEE/ASME Int. Conf. on Advanced Intelligent Mechatronics, 2001, pp. 69–74.
[20] S. Foong, K.-M. Lee, K. Bai, Harnessing embedded magnetic fields for angular sensing with nano-degree accuracy, IEEE/ASME Trans. Mechatronics (2011) 1–10.
[21] K.-M. Lee, R.A. Sosseh, Z. Wei, Effects of the torque model on the control of a VR spherical motor, Control Eng. Pract. 12 (2004) 1437–1449.
[22] K.-M. Lee, H. Son, Distributed multipole model for design of permanent-magnet based actuators, IEEE Trans. Magn. 43 (2007) 3904–3913.